PUBLICATIONS OF THE ASTRONOMICAL SOCIETY OF THE PACIFIC, **125**:1393–1404, 2013 November

Data Reduction and Early Science Calibration for FORCAST, A Mid-Infrared Camera for SOFIA

T. L. HERTER,[1] W. D. VACCA,[2] J. D. ADAMS,[1] L. D. KELLER,[3] J. SCHOENWALD,[1] L. HIRSCH,[1] J. WANG,[1] J. M. DE BUIZER,[2] L. A. HELTON,[2] AND M. C. LLORENS[2]

Received 2013 February 12; accepted 2013 September 25; published 2013 November 6

ABSTRACT. FORCAST is a mid-infrared (5–40 μm) facility instrument for the Stratospheric Observatory for Infrared Astronomy (SOFIA). After achieving first light flight in 2010 May, FORCAST has completed two observatory characterization flights and thirteen science flights on SOFIA. In this paper we describe the photometric calibration of FORCAST which involves some subtleties in correction for array artifacts and uncertainties due to the airborne environment. At present FORCAST is able to achieve approximately 20% (3σ) uncertainty in the calibration.

Online material: color figures

1. INTRODUCTION

The Faint Object infraRed CAmera for the SOFIA Telescope (FORCAST) is a wide-field camera facility instrument design for the Stratospheric Observatory For Infrared Astronomy (SOFIA) offering continuum and narrow band imaging in the infrared from 5–40 μm. Low-to-moderate resolution spectroscopic observations at these wavelengths will commence during SOFIA Cycle 1 using a suite of grisms in FORCAST. First light with SOFIA was achieved with FORCAST on 2010 May 26 (Gehrz et al. 2011). This was followed by two observatory characterization flights (OCF2 and OCF3) in 2010 November and three Short Science flights in 2010 December. A Basic Science program of ten flights with FORCAST were flown in 2011 May-June in support of the general community. A short description these flights and FORCAST are included with a series of publications on the short science flights (Young et al. 2012; Herter et al. 2012).

The goal of this paper is to discuss the acquisition, reduction, and photometric calibration of FORCAST data. Broadband astronomical instruments operating in the thermal infrared have a large photon background due to the atmosphere and telescope that places challenging demands on detector readout rates (to avoid saturation) and requires specialized acquisition sequences ("chopping" and "nodding"). Source signals are typically quite small compared to the background emission. For instance, the FORCAST 19.7 μm filter response to a flat-spectrum point source is ~1200 electrons/s/mJy spread over 30 pixels, while the background emission is about 1.3×10^9 electrons/s/pixel. Thus, for a 100 mJy source, the photo-electron rate from the background is 325,000 times larger than for the source. By design, the double difference of the chop-nod data removes this background signal (but not the noise component) so that high precision flat fielding is not required to accurately remove the background for photometric extractions. Flat fielding then needs only correct at a level consistent with the signal-to-noise ratio (S/N) on the source (and not that of the background).

A general description of FORCAST is given in § 2 and Herter et al. (2012). For design and performance details, see also Keller et al. (2002, 2004) and Adams et al. (2006, 2010, 2012b). For details on the design, fabrication, and lab testing of the grisms, see Ennico et al. (2006, 2007) and Deen et al. (2008). Data acquisition is discussed § 3.1. Subsequent sections cover removal of array artifacts such as droop, cross-talk, and nonlinearity (§ 3.2.2–3.2.3), calibration method, atmospheric corrections, color corrections, and selection and use of calibrators (§ 4). § 5 discusses limitations involved in FORCAST data reduction and calibration, the overall calibration uncertainty, and prospects for improvement.

2. INSTRUMENT DESCRIPTION

FORCAST is a two-channel cryogenic camera and spectrometer. The short wavelength channel (SWC) operates at 5–26 μm using a 256×256 pixel Si:As blocked inpurity band (BIB) detector, while the long wavelength channel (LWC) operates at 26–40 μm using a Si:Sb BIB detector of the same format. The field-of-view is $3.4' \times 3.2'$; after post-processing, the plate scale is $0.768''$/pixel. Dual channel imaging is enabled using a cold dichroic beamsplitter to split the telescope beam into the two FORCAST channels; however, the dichroic can be moved out of the beam to allow imaging in a single channel with higher

[1] Department of Astronomy, Space Sciences Building, Cornell University, Ithaca, NY 14853-6801
[2] Universities Space Research Association, NASA Ames Research Center, MS 211-3, Moffett Field, CA 94035
[3] Department of Physics, Ithaca College, Ithaca, NY 14850

throughput. Low-to-moderate resolution spectroscopy at 5–40 μm is possible using a suite of grisms.

The SWC and LWC arrays were designed and fabricated by DRS Technologies to operate under high and moderate thermal backgrounds experienced in flight. A switchable capacitance on the unit cell allows the user to choose the full well depth (1.8×10^7 or $1.9 \times 10^6 e^-$) depending on the level of thermal background. Both arrays have a quantum efficiency QE $\gtrsim 25\%$ over most of their used range. The detectors are bonded to a readout integrated circuit with a 16-channel output multiplexer. The 16 channels are read out simultaneously and later combined in hardware to produce 256×256 pixel images.

The optical prescriptions for the two channels are identical. Telescope focus is located inside the FORCAST CsI window at a field stop. A single hyperbolic mirror collimates the $f/19$ telescope beam and the collimated beam is folded to the dichroic slide where the beam is split into the SWC and the LWC, or directed entirely into the SWC or LWC. Each channel contains a Lyot stop and two tilted, aspheric, concave camera mirrors that produce images on the detectors at $f/5$. Each channel also contains a CdTe pupil viewing lens which can be rotated into or out of the beam at the front of the detector; the pupil viewers are used primarily to align the FORCAST collimator mirror with the telescope secondary mirror.

A slit wheel is located at the field stop that contains six slit and field options. For SOFIA Cycle 1, there are two long slits ($192'' \times 2.4''$ and $4.7''$), a short slit ($11.25'' \times 2.4''$), and a $3.4' \times 3.2'$ imaging field. The other two slit masks are test masks that are used to measure optical alignment, throughput, and distortion. Each channel contains two cryogenic wheels housing a total of ten broadband filters and grisms. These wheels straddle the Lyot stop in order to keep the filters and grisms near a pupil.

Table 1 lists the central wavelengths and bandwidths for the FORCAST filters. Herter et al. (2012) show the FORCAST filter transmission curves across the FORCAST wavelength region. Filters with wavelength <13 μm in the SWC are standard Optical Coating Laboratory, Inc. (OCLI) thin-film interference filters. These filters are stacked with blocking calcium flouride and barium flouride filters to prevent long wavelength light leaks. The 19.7 and 31.4 μm filters are also thin-film interference filters. The 24.2, 33.5, 34.8, and 37.1 μm filters are custom double half-wave (three mesh) filters procured from Lakeshore Cryotronics. These filters are double-stacked to improve out-of-band rejection. Although these filters have high transmission, they have significant blue (<5 μm) leaks which require large color corrections as part of the calibration (see § 4). The dichroic can be used to mitigate the blue leaks for the mesh filters in the LWC. In addition, we are procuring long pass mesh filters from Infrared Laboratories, Inc. to use as high transmission, blue light blockers for the Lakeshore mesh filters. For Cycle 1, we may use an interference filter at 25.2 μm ($\Delta\lambda = 1.8$ μm), recently procured from the University of Reading, in lieu of the 24.2 μm Lakeshore mesh filter since the 25.2 μm filter does not require a blocker.

TABLE 1
FORCAST FILTER PROPERTIES[a]

Channel	$\lambda_{\rm eff}$ (μm)	$\Delta\lambda$[c] (μm)	Background[b] dichroic ($Me^-/s/pix$)	Background[b] direct ($Me^-/s/pix$)
SWC	5.4	0.16	—	6.3
	6.4	0.14	—	15.2
	6.6	0.24	—	28.6
	7.7	0.47	—	210
	8.6	0.21	—	226
	11.1	0.95	380	525
	11.3	0.24	100	139
	19.7	5.5	1270	1390
	24.2	2.9	450	656
LWC	31.4	5.7	250	650
	33.5	1.9	54	118
	34.8	3.8	149	336
	37.1	3.3	70	174

[a] Not all of these filters will be available for Cycle 1 observations due to the installation of the grism suite.

[b] The background photo-electron given for altitudes $>41,000$ feet can vary by 20% under normal conditions.

[c] These are based on the half-power points of the filter profiles shown in Herter et al. (2012).

The dichroic was procured from Barr UK and is made from a silicon subtrate with mulitple CdSe and PbTe coatings. The dichroic throughput is ~60% from 5–10 μm, ~85% from 11–28 μm, and ~40% from 28–40 μm. Thus the increase in observing efficiency in dichroic mode is partially negated by a decrease in sensitivity performance in each channel.

Figure 1 shows the transmission curves for an ATRAN model atmosphere (Lord 1992), FORCAST filters and dichroic (transmission only), and the detector quantum efficiencies. The filter and dichroic curves were measured at room temperature. We have not completed dichroic reflectivity measurements for 5–26 μm; these measurements require special instrument configurations for in situ measurements with the grisms.

3. DATA ACQUISITION AND REDUCTION

3.1. Data Aquisition

For SOFIA, the observations are thermal background-limited. Unlike a space-based telescope, the warm atmosphere and warm telescope provide background emissions that limit the sensitivity floor. The high backgrounds demand fast detector read and reset rates to prevent saturation, typically 30–500 Hz for a full frame. As mentioned earlier, the typical source signal is about 10^{-4} the background. Therefore, as with ground-based IR observatories and unlike space-based observatories, chopping

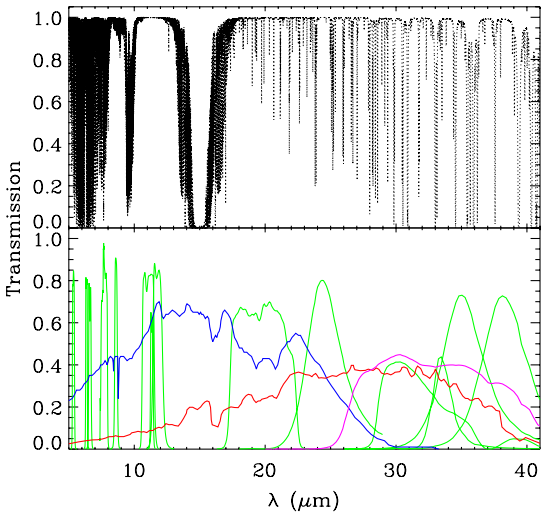

FIG. 1.—Atmospheric transmission and FORCAST throughput vs. wavelength. *Top panel*: atmospheric transmission for an altitude of 41,000 ft., precipitible water vapor of 7.1 μm, and an elevation angle of 40°. *Bottom panel*: throughput for the FORCAST filters (*green*), dichroic transmission (*magenta*), SWC quantum efficiency (*blue*) and LWC quantum efficiency (*red*). The reflectivity of the dichroic is not shown. The filter and dichroic transmission curves were measured at room temperature. See the electronic edition of the *PASP* for a color version of this figure.

and nodding are essential for obtaining scientifically useful mid-infrared data on SOFIA. Chopping with the secondary mirror is required to sample the sky background and subtract the sky emission from the source emission during data reduction. Nodding of the telescope is also required in order to subtract the noncommon path background present in a single pair of chop beams.

FORCAST drives the chop signal to the SOFIA chopper interface. The chop frequency is chosen to eliminate variations in thermal background of the sky, typically a few Hz, and the readout of the FORCAST arrays are synchronized with this signal. The individual frames taken in a particular chop beam are coadded in hardware (see Pirger et al. (2006) for a description of the detector control and acquisition hardware) on-the-fly. FORCAST efficiency depends in part on the number of "throw-away" frames which are discarded during the chop transistion and settle time. Higher frame rates result in better noise performance and increased efficiency in the chopping duty cycle. Therefore, we select the low-capacity well size whenever possible in order to read the array at high frame rates at $2/3$ full well depth.

The SOFIA chopping secondary can be configured for chopping symmetrically about the telescope's optical axis or asymmetric chopping with the on-source beam placed on the optical axis. For compact ($<120''$) sources, symmetric chopping is convenient and will place all four beams in the field-of-view (Fig. 3). Large chop throws incur optical coma in the beam ($2''$ for every $60''$ of chop throw); therefore asymmetric chopping is desirable for large ($>120''$), extended sources where a large chop throw is required to chop off the source into blank sky. Two chop-nod sequences are defined: C2N (symmetric chop and nod with all four beams in the field-of-view) and C2NC2 (asymmetric chop and nod with large chop and nod throws). C2N is usually performed with the nod throw matched to the chop throw (NMC configuration) or with the nod direction perpendicular to the chop direction (NPC configuration). NMC configuration has the advantage of coadding two beams in real time to boost S/N seen in each image, as well as reducing the effects of variations in flat field response by placing the two beams at the same location on the array. These modes are summarized in Table 2. Dither moves with the telescope can be performed between sequences for the removal of bad pixels during post-processing.

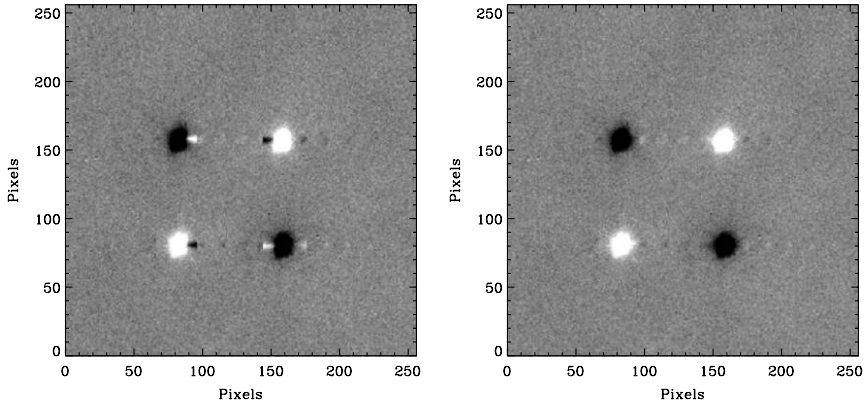

FIG. 2.—μ Cep at 11.1 μm showing the effects of droop (*left*) and with droop corrected (*right*). The images have been chop and nod subtracted (§ 3.2.4). Both images have also been corrected for crosstalk (§ 3.2.5) which does not correct droop. Note there remains a faint "echo" of the source (see the lower left image of Fig. 5 for a better illustration of this effect).

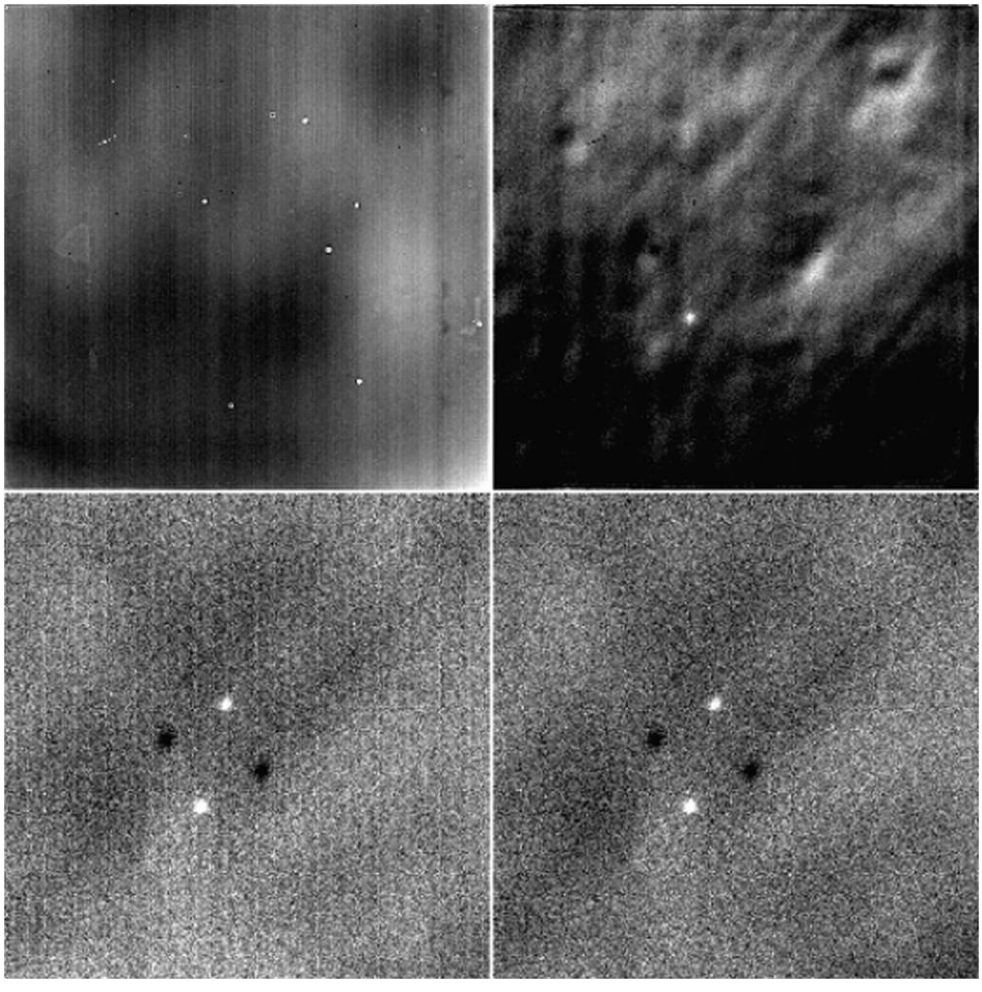

FIG. 3.—Nonlinearity correction factor vs. background signal per frame for LWC (*low capacitance, solid*), LWC (*high capacitance, dotted*) and SWC (*low and high capacitances, dashed*). The correction factor is normalized to a background of ~60% full well, or ~9000 instrumental digital units (ADU). Saturation occurs at 13,000–14,000 ADU. The gain values are $136e^-/\mathrm{ADU}$ for low capacitance and $1294e^-/\mathrm{ADU}$ for high capacitance.

3.2. Data Reduction

In the mid-infrared nonlinearity corrections are driven by the background signal level rather than source signal level. Ideally this correction can be eliminated by adjusting the readout rate of the detector to maintain the same integrated background level for all observations. However, in practice, low frame rates can increase array noise and reduction efficiency over a chop cycle. This means that the integrated background level cannot be the same for all filters but the level can be fixed for a given filter. Additionally, specific features or artifacts associated with the array must be corrected. The multiplexers used by FORCAST exhibit "droop" which causes the output voltages to sag when a signal is present and "cross-talk" which cause bright (or dark) pixels to echo through pixels sampled on the same output channel. Other calibration steps such as applying atmospheric and color corrections and reliance on astronomical calibrators are similar to those used for any astronomical camera. However, because the aircraft heading sets the azimuthal angle of an observation, a given calibrator is typically observed at a single elevation angle over a flight. Atmospheric correction of FORCAST data is presently limited to applying standard models but should improve when the on-board water vapor monitor is operational. Color corrections are based upon (the sometimes

TABLE 2

FORCAST DATA ACQUISITION MODES

Mode	Pattern	Description[a]
C2N	NPC	symmetric chop with nod perpendicular chop direction
C2N	NMC	symmetric chop with matched nod along chop
C2NC2		asymmetric chop, source on optical axis[b]

[a] Symmetric and asymmetric refer to two chop source positions relative to the optical axis of the telescope.

[b] Gives best image quality for extended sources but only the on-axis position of the four chop-nod beams contains the source.

limited knowledge of) system response curves but are supplemented with empirical data from blue and red calibrators. A final complication is that the bright calibrators needed for FORCAST are typically evolved stars with dust shells which typically exhibit long period variability.

There are a number of steps involved in the reduction of FORCAST data. Data are reduced for a sequence of observations in a given filter and dichroic mode. § 3.2.1–§ 3.2.10 each describe a step in the data reduction process and are arranged in the order in which the implemented pipeline applies each step. We did not implement flat field corrections in the pipeline for Early Science; flat fielding is discussed in § 5.1.

3.2.1. Bad Pixel Correction

Independently generated bad pixel masks are used to mark bad pixel values to be corrected. Bad pixels are identified as outliers to the median pixel value of a moving box window across a raw image. Typically, these bad pixels are "dark" (low or missing signal in response to illumination). A surface function is fit to the global variations across the raw images. Interpolation over bad pixels is then performed using the surface function as a reference and the bad pixel values are replaced with the interpolated values.

3.2.2. Droop Correction

The BIB detector readout integrated circuits exhibit suppression of a signal caused by the presence of the signal itself. We refer to this effect as "droop" and fortunately it is corrected via a simple algorithm. A pixel value p_i is corrected to a value $p_{i,\mathrm{corr}}$ by adding a fractional offset of the total signal in all 16 detector multiplexer output channels read simultaneously with p_i:

$$p_{i,\mathrm{corr}} = p_i + f \sum_{i=1}^{16} p_i \tag{1}$$

where f is the droop fraction, typically a value of 0.0035. This correction is applied to the whole image. Figure 2 shows an image where the effects of droop on a point source are visible and the same image with droop corrected.

3.2.3. Nonlinearity Correction

Direct-injection circuitry in the unit cell provides an intrinsically linear response (by keeping the detector bias constant). However, there is a residual nonlinearity which manifests itself as an increase in response with increasing well depth (set by the thermal background) until saturation is approached. This nonlinearity is not fully understood but it can be mitigated by acquiring all data at the same well depth. Unfortunately this is not always possible due to limits in frame rate selection which is both quantized and limited to the 30–600 Hz range. The highest frame rate is set by the readout electronics (the array can operate up to 1 kHz). Array performance degrades at lower frame rates, mainly due to the increased effect of bad pixels on the array (the effect being an increase in read noise). Thus, generally, a nonlinear correction will need to be applied. The system nonlinearity is characterized in the lab by illuminating the array with a point source of fixed brightness and then varying the frame rate to give a range of background levels from a low well depth to near full well depth. This enables us to apply a nonlinearity correction to data taken at any well depth (Fig. 3). The average well depth for the data is determined and the pixel values are corrected to a linear response with respect to a well depth of approximately 60% full well for a given camera channel and capacitance. In practice, we attempt to take all data near 60% full well (determined to be the optimum location for S/N performance). Exceptions include observing bright, extended sources that cause array offsets to vary; acquisition at lower well depths ($\lesssim 40\%$) reduces this effect.

3.2.4. Chop and Nod Subtraction

After droop correction, chop subtraction is applied to each chop pair. In C2N mode, the chop pair differences are then subtracted (nod subtraction). In C2NC2 mode, chop pairs are differenced, followed by a subtraction of the off-source pair difference from each adjacent (in time) on-source chop pair. Figure 4 shows a coadded raw image, chop-subtracted, and nod-subtracted images. Data are acquired in a standard chop-nod sequence with a typical chop-nod cycle with 15 s of integration time in each chop beam.

3.2.5. Crosstalk Correction

Crosstalk in the readout integrated circuit occurs while clocking over a feature with high contrast to the background, such as a bright point source or bad (dark) pixel. Following this feature, the signal contains a latent residual in each detector multiplexer readout channel and results in vertically-orientated (in image space) correlated noise which is seen in the chop-nod differenced images. The correction of crosstalk is accomplished using a row median subtraction algorithm: The median value of a readout multiplexer channel across a row is subtracted from each pixel in that readout multiplexer channel in that row. This algorithm works well for faint sources. Bright sources are somewhat problematic since they cause an additional ringing in the array in a way that is not fully removed by the median subtraction algorithm, an effect still being investigated. The additional ringing can be removed by dithering in field angle. Figure 5 shows examples of crosstalk seen in flight data and the data after crosstalk correction. For extended sources, the source is first removed using a box-median filter subtraction and then re-added after crosstalk correction is applied to the source-subtracted image.

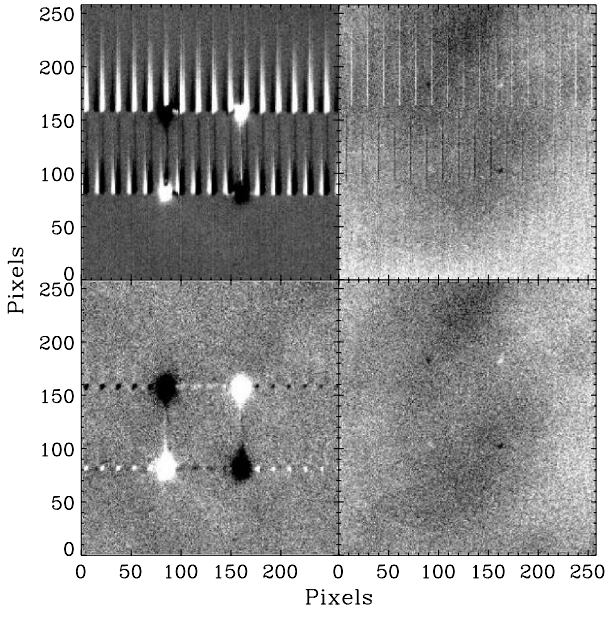

FIG. 4.—Sample processing of FORCAST chop-nod sequence at 31.4 μm on γ Dra (16.5 Jy) with chop and nod amplitudes of one arcminute. *Upper left*: raw image containing sky and telescope background. *Upper right*: chop subtracted data which removes most background emission. *Lower left*: chop and nod subtracted which removes the noncommon path background present in the chop-only subtracted image. *Lower right*: crosstalk-corrected data (see § 3.2.5). Over large scales the standard deviations are 45, 0.089, 0.039 and 0.036 Jy/pix, respectively. The bright pixels on the source are about 300 mJy. The positive and negative images of the source each have a S/N of about 15 in the final image. The wall clock time for the observation is approximately 30 s per nod position. In the final image, large scale structure with a peak-to-peak amplitude of approximately 40 mJy occurs due to background changes over the chop-nod sequence.

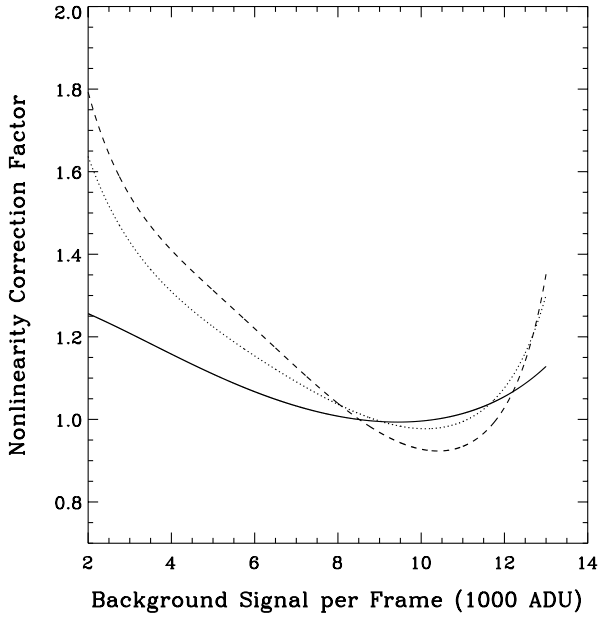

FIG. 5.—Crosstalk from a bright source and bad pixels. All these images have been corrected for droop (§ 3.2.2) and have been chop and nod subtracted (§ 3.2.4). *Upper Left*: μ Cep at 11.1 μm showing the vertically-orientated crosstalk resulting from a spike in detector output channel signal. *Lower Left*: μ Cep at 11.1 μm (1700 Jy) after crosstalk correction. Some residual is seen for very bright sources such as μ Cep at 11.1 μm. *Upper Right*: α Cet at 31.4 μm (25 Jy) showing crosstalk caused by bad pixels. *Lower Right*: α Cet at 31.4 μm after crosstalk correction.

3.2.6. Scaling Data to Photo-Electron Rates

After nonlinearity correction, the data are scaled from digital instrument units to units of photo-electron rate ($Me^-/\mathrm{s/pixel}$) based on the image values (digital instrument units per pixel per readout frame), the full frame readout rate, and the gain from e^- to digital instrument units resulting from the selected integration capacitance at the detector unit cell.

3.2.7. Image Rectification

After nonlinearity correction the images are corrected for optical distortion. The off-axis nature of the FORCAST optical path results in anamorphic magnification (~6%) and nonlinear distortion (~1%); both are rectified simultaneously by the pipeline. The optical distortion is measured in the lab using a square grid of point sources (illuminated by the room thermal background) located at the FORCAST field stop. A polynomial warping function is fit to the positions of the sources and is then used to rectify the FORCAST images so that proper astrometry can be applied to the final, processed images. The rectified images are 262×247 pixels with a plate scale of 0.768″ per pixel, yielding a field-of-view of approximately $3.4' \times 3.2'$. The algorithm achieves good performance: It rectifies the pinhole grid to within 0.07 pixels in the SWC and 0.19 pixels in the LWC (Adams et al. 2012b). In the OMC-2 field observed during Early Science (Adams et al. 2012a), astrometric residuals for several point sources across the field were 0.38″ for both 19.7 and 37.1 μm.

3.2.8. Beam Merge

In a each rectified image, the on-source beams are aligned by shifting them according to the chop and nod throws and angles that were commanded for the observations. For a compact source with all four beams located in the field-of-view in NPC or NMC mode, this means the four beams are aligned and averaged, resulting in a single image of the source with S/N 2 times higher than a single chop and nod beam.

3.2.9. Field Rotation

The FORCAST data reduction pipeline uses the field angle reported by the observatory to rotate the images to a common field angle (i.e., northern direction is vertical upwards, eastern direction is to the left) for all merged images. Figure 6 shows a merged image after field rotation to the correct orientation.

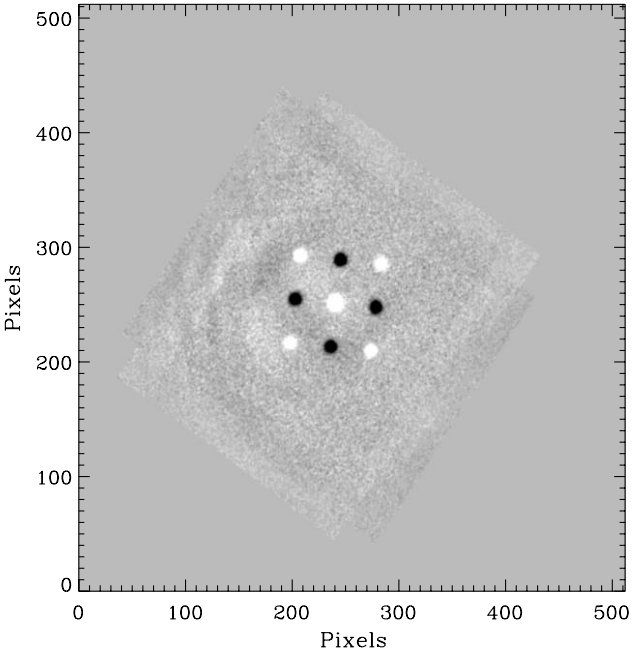

FIG. 6.—Image of γ Dra at 11.3 μm, from Basic Science Flight 64, after beam merging, field rotation, and previous reduction steps. The image of the star at the center of the beam pattern is the averaged signal in all beams after alignment of the beams using the chop and nod throw and angle parameters and change of sign to make negative beams positive. In this image, the northern direction is vertical upwards and the eastern direction is towards the left.

3.2.10. Image Alignment and Averaging

The sequence of rotated images are aligned for averaging using one of three methods. If a point source is available, the position of the point source in each image is used to shift each image to align the point source over the sequence. For an extended source, a cross-correlation algorithm is used to determine the optimum offsets with which to shift the images based on the measured correlation coefficients with respect to the first image in the sequence. If the source is too faint to be seen in a single merged and rotated image, the images are aligned using the telescope pointing sky coordinates reported from the observatory.

The aligned images are then combined with averaging, reducing the noise which scales with the square root of the total integration time over the stack of observations in the given filter/dichroic mode.

4. PHOTOMETRIC CALIBRATION

Here we outline the process of determining the calibration factors that convert the count rates (in Me^{-}/s) recorded in the images into physical flux densities (in Jy). Once determined, the calibration factors are written into the headers of the data files and the modified files are ingested into the SOFIA archive as Level 3 data products. It should be noted that nothing is done to the actual data values in the images between Level 2 and Level 3; the only differences between the Level 2 and Level 3 data products are the addition of keywords to the headers of the Level 3 files containing the calibration factor, its uncertainty, and the reference wavelength.

The determination of the conversion factors began with the calculation of the predicted fluxes for a small set of standards stars. The predicted fluxes were computed by multiplying the model stellar spectrum by the overall filter+instrument+telescope+atmosphere response curve and integrating over the filter passband to compute the mean flux in the band (see below). The adopted filter throughput curves were those provided by the vendor or measured by us, modified to remove regions (around 6–7 microns and 15 microns) where the values were contaminated by noise. As mentioned in § 2, the filter and dichroic transmission curves were measured at room temperature. Updated cold dichroic transmission and reflection curves may be available for Cycle 1. The instrument throughput was calculated by multiplying the transmission curves of the entrance window, dichroic, internal blockers, mirrors, and the detector responsive quantum efficiency. The telescope throughput value was assumed to be constant (85%) across the entire FORCAST wavelength range. The atmospheric transmission was computed using the ATRAN code (Lord 1992) for a range of observatory altitudes (corresponding to a range of overhead precipitable water vapor values) telescope elevations (see below).

For most of the standard stars, the adopted stellar models were obtained from the Herschel calibration group and consist of high-resolution theoretical spectra, generated from the MARCS models (Gustafsson et al. 1975; Plez et al. 1992), scaled to match absolutely calibrated observational fluxes (Dehaes et al. 2011). The uncertainties in the stellar models are expected to be on the order of 5–10% (Dehaes et al. 2011). For β UMi we scaled the model by a factor of 1.18 in agreement with the results of the Herschel calibration group (J. Blommaert, private communication) (The newer version of the model from the Herschel group has incorporated this factor.) For μ UMa, we used the Cohen et al. (1996) model, extended with an Engelke (1992) function and the parameters given by Cohen et al. (1996) to cover the entire FORCAST wavelength range. For μ Cep, we adopted the ISO spectrum from AOT 08001274.[4] The theoretical spectra of Pallas and Europa were computed by T. Müller (private communication) for the dates and times of the SOFIA observations using the thermophysical model of Müller & Lagerros (1998, 2002).

[4]There are three spectra of μ Cep available in the ISO archives (see Sloan et al. 2003). Unfortunately, the flux levels in these spectra differ by up to 20% from each other. Given that μ Cep is a known variable star, this is probably not surprising. However, this fact does call into question the use of μ Cep as an infrared "standard star". We chose the spectrum that gave the best agreement with the IRAS fluxes for the star at 12 and 25 microns. This spectrum also had the highest S/N of the three and did not exhibit any spectral discontinuities.

The predicted mean flux of an object with a spectrum $F_\lambda(\lambda)$ in a passband is given by Tokunaga & Vacca (2005),

$$\langle F_\lambda \rangle = F_\lambda(\lambda_{\rm iso}) = \frac{\int \lambda F_\lambda(\lambda) S(\lambda) d\lambda}{\int \lambda S(\lambda) d\lambda}, \quad (2)$$

where $S(\lambda)$ is the total system throughput (including the atmosphere, the telescope, the filter, the instrument optics, and the detector) and $F_\lambda(\lambda_{\rm iso})$ is the stellar flux (above the atmosphere) at the isophotal wavelength $\lambda_{\rm iso}$. The mean wavelength of the passband (including the dichroic) is given by

$$\langle \lambda \rangle = \frac{\int \lambda S(\lambda) d\lambda}{\int S(\lambda) d\lambda}. \quad (3)$$

The mean flux in frequency units can be computed from the mean flux in wavelength units using the equation

$$\langle F_\nu \rangle = \langle F_\lambda \rangle \lambda_{\rm piv}^2 / c \quad (4)$$

where

$$\lambda_{\rm piv} = \left[\frac{\int \lambda S(\lambda) d\lambda}{\int \frac{S(\lambda)}{\lambda} d\lambda} \right]^{0.5} \quad (5)$$

is the pivot wavelength. The pivot wavelength provides the rigorously correct conversion between mean flux in wavelength units and mean flux in frequency units for a photometric measurement over a passband. The mean and pivot wavelengths and fluxes for the standard stars computed in this way are given in Table 1 for both single and dichroic modes.

Following the standard practice of IRAS, ISO, and Spitzer, the quoted fluxes in FORCAST images refer to a nominal "flat spectrum" source, for which $F_\lambda \sim \lambda^{-1}$ and $F_\nu \sim \nu^{-1}$ (and therefore $\lambda F_\lambda = \nu F_\nu =$ constant), at a reference wavelength $\lambda_{\rm ref}$. The number of electrons detected per second from a source is given by

$$N_{e^-} = \int \lambda F_\lambda(\lambda) S(\lambda) d\lambda / hc = \frac{1}{hc} \langle F_\lambda \rangle \int \lambda S(\lambda) d\lambda = \langle F_\lambda \rangle R_\lambda, \quad (6)$$

where

$$R_\lambda = \frac{1}{hc} \int \lambda S(\lambda) d\lambda \quad (7)$$

is the system response, which is independent of the source properties. The number of electrons detected per second from a source with the nominal spectrum is then given by

$$N_{e^-}^{\rm nom} = \int \lambda F_\lambda^{\rm nom}(\lambda) S(\lambda) d\lambda / hc \quad (8)$$

$$= \frac{1}{hc} \frac{\lambda_{\rm ref}}{\langle \lambda \rangle} F_\lambda^{\rm nom}(\lambda_{\rm ref}) \int \lambda S(\lambda) d\lambda \quad (9)$$

$$= \frac{\lambda_{\rm ref}}{\langle \lambda \rangle} F_\lambda^{\rm nom}(\lambda_{\rm ref}) R_\lambda, \quad (10)$$

where we have assumed $\lambda F_\lambda^{\rm nom}(\lambda) = \lambda_{\rm ref} F_\lambda^{\rm nom}(\lambda_{\rm ref})$. Using equation (6) for a standard star and equation (8) for the object, and taking $N_{e^-}^{\rm nom} = N_{e^-}^{\rm obj}$, we have

$$F_\lambda^{\rm nom,obj}(\lambda_{\rm ref}) = \frac{N_{e^-}^{\rm obj}}{N_{e^-}^{\rm std}} \frac{\langle \lambda \rangle}{\lambda_{\rm ref}} \langle F_\lambda^{\rm std} \rangle. \quad (11)$$

We can convert the nominal flux in wavelength units at the reference wavelength to the flux in frequency units at that wavelength with

$$F_\nu(\lambda_{\rm ref}) = F_\lambda(\lambda_{\rm ref}) \lambda_{\rm ref}^2 / c \quad (12)$$

and the pivot wavelength. With these we have

$$F_\nu^{\rm nom,obj}(\lambda_{\rm ref}) = \frac{N_{e^-}^{\rm obj}}{N_{e^-}^{\rm std}} \frac{\langle \lambda \rangle \lambda_{\rm ref}}{\lambda_{\rm piv}^2} \langle F_\nu^{\rm std} \rangle. \quad (13)$$

The flux in frequency units calculated with this equation therefore refers to a flat spectrum source at the reference wavelength.

The above equations assume that the transmission function $S(\lambda)$ is the same for the observations of the standard and the object. However, because of the variation in the atmospheric transparency as a function of airmass and water vapor, this will not generally be the case for SOFIA observations. We can account for this by scaling the transmission to a "reference" atmospheric transmission, taken to be that for 41 k feet and a 45° telescope elevation angle. Expressing the above equations in terms of this reference transmission,

$$R_\lambda^{\rm ref} = \frac{1}{hc} \int \lambda S^{\rm ref}(\lambda) d\lambda, \quad (14)$$

we have

$$F_\nu^{\rm nom,obj}(\lambda_{\rm ref}) = \frac{N_{e^-}^{\rm obj}}{N_{e^-}^{\rm std}} \frac{\langle \lambda \rangle \lambda_{\rm ref}}{\lambda_{\rm piv}^2} \frac{R_\lambda^{\rm std}/R_\lambda^{\rm ref}}{R_\lambda^{\rm obj}/R_\lambda^{\rm ref}} \langle F_\nu^{\rm std} \rangle. \quad (15)$$

We computed the ratio $R_\lambda / R_\lambda^{\rm ref}$ for a range of altitudes (corresponding to a range of water vapor values for a standard atmosphere) and telescope elevation angles for each filter using ATRAN. We assumed that the ratio was separable into two independent functions of airmass, X and aircraft altitude, h,

$$\frac{R_\lambda}{R_\lambda^{\rm ref}} = f(X) g(h) \quad (16)$$

and fit the calculated ratios with low order polynomials to determine $f(X)$ and $g(h)$ where $X = 1.414$ and $h = 41$ k for the reference. Figure 7 shows examples of these fits. With these fits, the ratio of the response values was determined for the airmass and altitude of the aircraft during the observations. Then using equation (15), the nominal flux of an object at the reference wavelength and at the reference altitude and airmass was determined.

An observer often wishes to determine the true flux of an object at the reference wavelength, rather than the flux of an equivalent nominal flat-spectrum source. The color corrections K needed for this conversion are defined such that

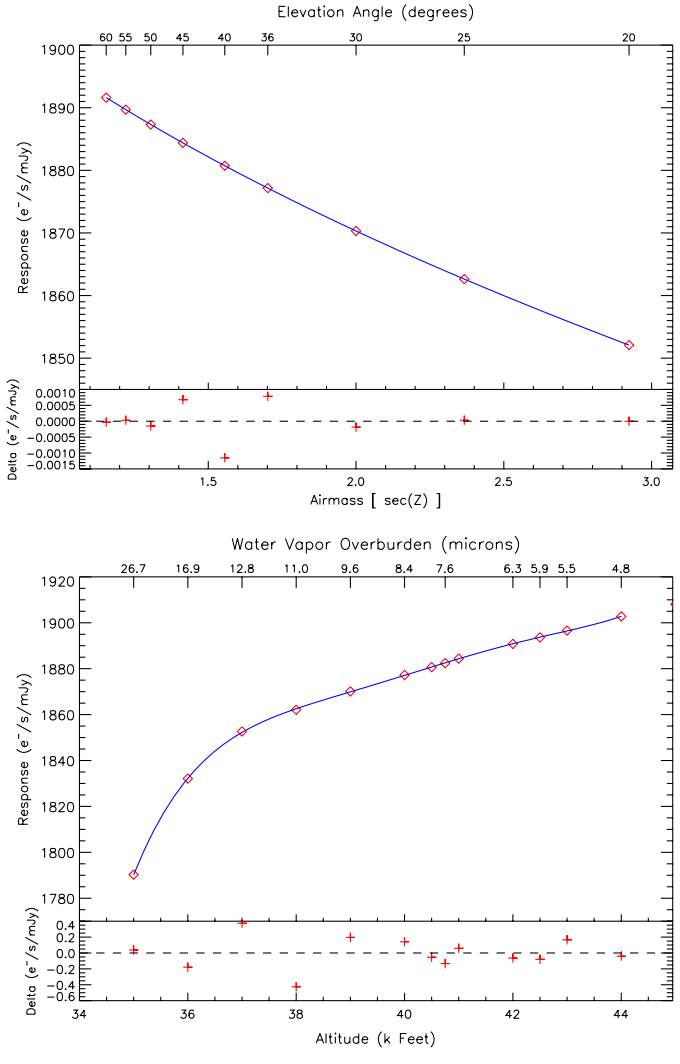

FIG. 7.—Response vs. airmass and altitude derived from ATRAN model sampling for 24.2 μm. The solid blue line is a lower order polynomial fit the data points (*diamonds*) derived from the models. See the electronic edition of the *PASP* for a color version of this figure.

$$K = \frac{F_\nu^{\rm nom,obj}(\lambda_{\rm ref})}{F_\nu^{\rm obj}(\lambda_{\rm ref})}. \tag{17}$$

Since

$$F_\nu^{\rm nom,obj}(\lambda_{\rm ref}) = \frac{\langle\lambda\rangle\lambda_{\rm ref}}{\lambda_{\rm piv}^2}\langle F_\nu^{\rm obj}\rangle, \tag{18}$$

we have

$$K = \frac{\langle\lambda\rangle\lambda_{\rm ref}}{\lambda_{\rm piv}^2}\frac{\langle F_\nu^{\rm obj}\rangle}{F_\nu^{\rm obj}(\lambda_{\rm ref})}. \tag{19}$$

The values of K can then be computed for any assumed shape of the input spectrum. For most filters and spectral shapes, the color corrections are fairly small ($<10\%$). Our calculated color corrections for power law and blackbody-shaped input spectra are listed in Table 3.[5] By dividing the nominal flux by the value of K for an assumed spectral shape, the true flux of the object at the reference wavelength can be estimated.

With the predicted fluxes of the standards in hand, the reduced images of the standards (including two asteroids, Pallas and Europa) observed on the flights were analyzed. Photometry was measured on these images using an aperture of 12 pixels and a background region of 25–35 pixels. The measured count rates were then used to compute the calibration factor for converting 1 $\rm Me^-/s$ in a reduced FORCAST image into Jy,

$$C = \frac{N_{e^-}^{\rm obj}}{F_\nu^{\rm nom,obj}(\lambda_{\rm ref})} = \frac{N_{e^-}^{\rm std}}{\langle F_\nu^{\rm std}\rangle}\frac{\lambda_{\rm piv}^2}{\langle\lambda\rangle\lambda_{\rm ref}}\frac{R_\lambda^{\rm obj}/R_\lambda^{\rm ref}}{R_\lambda^{\rm std}/R_\lambda^{\rm ref}} \tag{20}$$

Each observation of a standard provided a value of the calibration factor in the various filters. The values of C were examined across all of the Basic Science flights to check for consistency. Discrepant values signaled problems with the standard star data and those images were then excluded from the calibration process. During this checking process it was noticed that the calibration factors derived from nondichroic observations of red standards (μ Cep, Pallas, and Europa) in the 24, 33, 34, and 37 μm filters were systematically different from those derived for the same filters from blue standard stars. We believe this is due to blue leaks in these long wavelength mesh filters, which results in higher count rates than expected for blue sources. To account for this sensitivity to color, the mean differences in the calibration factors for red and blue sources were computed and the resulting values were incorporated into the reported calibration factors derived from the blue standards observed in non-dichroic mode. (That is, the values of C

[5] Our calculated values for K will be updated for Cycle 1 pending new blocking filter performance and cold dichroic reflectivity knowledge.

TABLE 3
COLOR CORRECTIONS K FOR EARLY SCIENCE CALIBRATION[A,B]

	Single channel $\langle\lambda\rangle$ (μm)												
	5.356	6.348	6.614	7.702	8.609	11.089	11.344	19.670	24.158	31.383	33.415	34.688	37.087
$\alpha = -3$	1.000	1.000	1.000	1.000	1.000	1.001	1.000	1.007	1.005	1.004	1.003	1.003	1.003
$\alpha = -2$	1.000	1.000	1.000	1.000	1.000	1.000	1.000	1.000	1.000	1.000	1.000	1.000	1.000
$\alpha = -1$	1.000	1.000	1.000	1.000	1.000	1.000	1.000	1.000	1.000	1.000	1.000	1.000	1.000
$\alpha = 0$	1.000	1.000	1.000	1.000	1.000	1.001	1.000	1.008	1.009	1.005	1.004	1.005	1.007
$\alpha = 1$	1.000	1.000	1.000	1.001	1.000	1.002	1.000	1.028	1.044	1.016	1.018	1.025	1.037
$\alpha = 2$	1.001	1.000	1.001	1.002	1.000	1.004	1.000	1.071	1.171	1.044	1.064	1.098	1.171
$\alpha = 3$	1.001	1.000	1.001	1.004	1.001	1.007	1.000	1.166	1.673	1.134	1.259	1.436	1.846
$T = 10000$ K	1.001	1.000	1.001	1.002	1.000	1.004	1.000	1.067	1.157	1.042	1.060	1.091	1.158
$T = 5000$ K	1.000	1.000	1.001	1.002	1.000	1.004	1.000	1.064	1.143	1.040	1.056	1.085	1.146
$T = 1000$ K	1.000	1.000	1.000	1.001	1.000	1.002	1.000	1.040	1.061	1.028	1.033	1.046	1.073
$T = 500$ K	1.000	1.000	1.000	0.999	1.000	1.000	1.000	1.019	1.018	1.018	1.018	1.022	1.030
$T = 300$ K	1.001	1.000	1.000	0.999	1.000	0.999	1.000	1.001	1.001	1.010	1.008	1.010	1.010
$T = 100$ K	1.024	1.007	1.015	1.037	1.005	1.019	1.001	1.004	0.995	0.991	0.994	0.993	0.993
$T = 70$ K	1.056	1.018	1.037	1.095	1.013	1.058	1.003	1.079	1.018	0.995	0.998	0.995	0.996
$T = 50$ K	1.122	1.040	1.083	1.218	1.030	1.144	1.009	1.278	1.079	1.025	1.013	1.012	1.008
	Dual channel $\langle\lambda\rangle$ (μm)												
	5.356	6.348	6.614	7.702	8.609	11.089	11.344	19.670	24.158	31.360	33.576	34.674	37.000
$\alpha = -3$	1.000	1.000	1.000	1.000	1.000	1.001	1.000	1.007	1.005	1.004	1.001	1.002	1.002
$\alpha = -2$	1.000	1.000	1.000	1.000	1.000	1.000	1.000	1.000	1.000	1.000	1.000	1.000	1.000
$\alpha = -1$	1.000	1.000	1.000	1.000	1.000	1.000	1.000	1.000	1.000	1.000	1.000	1.000	1.000
$\alpha = 0$	1.000	1.000	1.000	1.000	1.000	1.001	1.000	1.008	1.009	1.004	1.001	1.003	1.002
$\alpha = 1$	1.000	1.000	1.000	1.001	1.000	1.002	1.000	1.028	1.044	1.011	1.004	1.008	1.008
$\alpha = 2$	1.001	1.000	1.001	1.002	1.000	1.000	1.000	1.071	1.171	1.023	1.011	1.023	1.029
$\alpha = 3$	1.001	1.000	1.001	1.004	1.001	1.007	1.000	1.166	1.673	1.044	1.038	1.071	1.119
$T = 10000$ K	1.001	1.000	1.001	1.002	1.000	1.004	1.000	1.067	1.157	1.023	1.010	1.022	1.027
$T = 5000$ K	1.000	1.000	1.001	1.002	1.000	1.004	1.000	1.064	1.143	1.022	1.010	1.021	1.025
$T = 1000$ K	1.000	1.000	1.000	1.001	1.000	1.002	1.000	1.040	1.061	1.018	1.007	1.015	1.015
$T = 500$ K	1.000	1.000	1.000	0.999	1.000	1.000	1.000	1.019	1.018	1.014	1.004	1.010	1.009
$T = 300$ K	1.001	1.000	1.000	0.999	1.000	0.999	1.000	1.001	1.001	1.009	1.003	1.007	1.006
$T = 100$ K	1.024	1.007	1.015	1.037	1.005	1.019	1.001	1.004	0.995	0.992	0.998	0.995	0.997
$T = 70$ K	1.056	1.018	1.037	1.095	1.013	1.058	1.003	1.079	1.018	0.995	0.998	0.996	0.996
$T = 50$ K	1.122	1.040	1.083	1.218	1.030	1.144	1.009	1.278	1.079	1.022	1.004	1.007	1.003

[a] The factor K converts an input flux density to that of a flat spectrum source. The input spectral shape is described by that of a power law ($F_\nu \propto \nu^\alpha$) or a blackbody with temperature T.
[b] These values will be updated for Cycle 1 pending the implementation of new blocking filters.

derived from these blue stars were divided by these leak correction factors.) The correction factors are listed in Table 4. These leak correction factors should also be applied to the measured count rates from any blue science targets (such as normal stars).

For each image, the observations of the standard obtained at the same altitude were used to derive the value of the calibration factor. In the few cases where there were multiple standards at the same altitude, the standard exhibiting the smallest uncertainty in the measured flux values (and therefore usually having the highest S/N) was chosen.

5. LIMITATIONS AND FUTURE PROSPECTS

5.1. Flat Fielding

We have measured the flat field response in three different ways for each filter passband. Because of time limitations it was not possible to map a point source across the focal plane in-flight. First, FORCAST contains an external lens that images an extended, uniform, precision-controlled thermal source onto the pupil of FORCAST (Adams et al. 2008, 2010). These flats can be taken in-flight alongside science observations. Second,

TABLE 4
MESH FILTER LEAK CORRECTION FACTORS FOR RESPONSES IN SINGLE CHANNEL (NON-DICHROIC) MODE.

$\langle\lambda\rangle$ (μm)	5.356	6.348	6.614	7.702	8.609	11.089	11.344	19.670	24.158	31.383	33.415	34.688	37.087
Correction	1.0	1.0	1.0	1.0	1.0	1.0	1.0	1.0	1.73	1.0	1.71	1.49	1.62

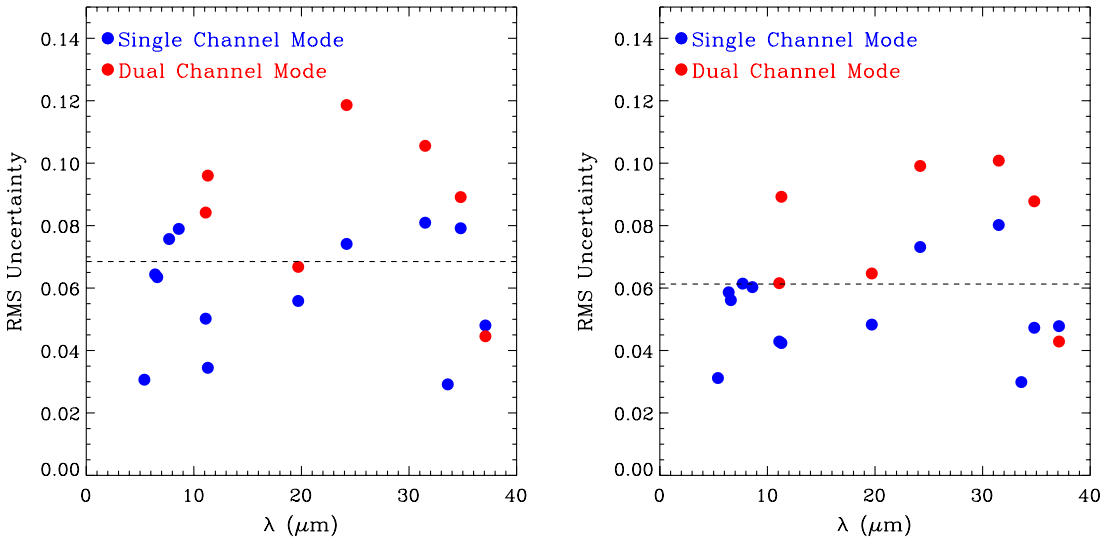

FIG. 8.—Standard deviation (RMS uncertainty) of the FORCAST normalized calibration response relative to the mean calibration response vs. filter wavelength and dichroic mode. Only data with S/N of 30–1000 and well depths below 83% (11,000 DN) were included. No data from flight 56 were included due to the resulting systemically low responses for that flight in all cases. *Left*: RMS uncertainty in the responses relative to the mean responses that were derived from all thirteen Early Science flights. The dashed line shows the overall RMS uncertainty for all filters. *Right*: RMS uncertainty for the calibration responses that are normalized to the mean calibration response for each individual flight. All data have been corrected for variations in altitude and elevation angle using ATRAN model atmospheres as references. Calibration on a flight-by-flight basis improves the uncertainty from ~6.8% to 6.1%. See the electronic edition of the *PASP* for a color version of this figure.

we have constructed flats using median raw (unsubtracted) images (the raw images are dominated by the thermal background which we assume is uniform at the focal plane). Finally, we have mapped the flat field using point sources that were dithered across the field in the lab. This method of flat fielding relies on an external foreoptics imaging system (Adams et al. 2010) that is not used in flight. In all methods, the observed peak-to-peak global response variations over the field-of-view is ~10–20%.

Using these constructed flat field images, we have examined the performance of flat fielding during pipeline processing. Overall, flat fielding failed to consistently reduce the photometric scatter of early science stellar calibrators, including bright calibrators such as Alpha Boo, at 11.1 and 31.4 μm. Work is ongoing to resolve this issue. For this reason, flat fielding was not used during early science data reduction. Note that dithering can improve the photometric uncertainties caused by variations in the flat field response.

5.2. Calibration Uncertainty

The uncertainties in calibration are caused by uncertainties in stellar models (see § 4), water vapor, variations in flat field response, and standard photometric uncertainty. Figure 8 shows the RMS uncertainty in the normalized calibration response versus filter wavelength and dichroic mode, with a comparison between normalization to the overall mean calibration responses for all thirteen flights or to the mean responses for each individual flight. All data were corrected for variations in altitude and elevation angle using ATRAN model atmospheres as references. Calibration on a flight-by-flight basis, instead of calibration using the overall mean responses for all flights, reduces the overall uncertainty from 6.8% to 6.1%. Table 5 lists the standard deviation of the normalized flux density to the mean calibration flux density (normalized for each flight) for each calibrator in all filters. μ Cep has the largest variation in calibration response among stellar calibrators, while Europa has the larger variation among non-stellar calibrators.

TABLE 5

RMS UNCERTAINTIES IN CALIBRATION RESPONSE[a]

Calibrator	N	RMS uncertainty
α Boo	126	0.069
α Cet	11	0.049
β And	28	0.088
β Peg	69	0.055
β Umi	3	0.068
γ Dra	65	0.064
μ Cep	125	0.102
α CMa	7	0.054
Pallas	15	0.068
Europa	3	0.113

[a]Standard deviation as determined from N observations per calibrator object selected from 452 total Early Science calibration observations after rejection. This observation set includes detections with S/N of 30–1000, well depth less than 83% (11,000 DN), and does not include any observations from flight 56 which showed systematically reduced throughput

5.3. Future Improvements to Calibration

The implementation of a water vapor monitor on SOFIA (Roellig et al. 2012) will provide an accurate measurement of the water vapor overburden. This will likely improve the FORCAST calibration accuracy since the current water vapor correction relies on an ATRAN model value associated with a given altitude.

Long-pass blocking filters for the Lakeshore mesh filters (24.2, 33.5, 34.8, and 37.1 μm) will be implemented for Cycle 1, thus eliminating the short wavelength light leaks. This will improve knowledge of the color correction factors, particularly for blue sources.

This work is based on observations made with the NASA/DLR Stratospheric Observatory for Infrared Astronomy (SOFIA). SOFIA science mission operations are conducted jointly by the Universities Space Research Association, Inc. (USRA), under NASA contract NAS2-97001, and the Deutsches SOFIA Institut (DSI) under DLR contract 50 OK 0901. Financial support for FORCAST was provided by NASA through award 8500-98-014 issued by USRA.

REFERENCES

Adams, J. D., Herter, T. L., Gull, G. E., et al. 2008, Proc. SPIE, 7014, 80
———. 2010, Proc. SPIE, 7735, 10
———. 2012b, Proc. SPIE, in press
Adams, J. D., Herter, T. L., Keller, L. D., et al. 2006, Proc. SPIE, 6269, 626911
Adams, J. D., Herter, T. L., Osorio, M., et al. 2012a, ApJ, 749, 6
Cohen, M., Witteborn, F. C., Carbon, D. F., Davies, J. K., Wooden, D. H., & Bregman, J. D. 1996, AJ, 112, 2274
Deen, C. P., Keller, L., Ennico, K.A., et al. 2008, Proc. SPIE, 7014, 81
Dehaes, S., Bauwens, E., Decin, L., et al. 2011, A&A, 533, 107
Engelke, C. W. 1992, AJ, 104, 1248
Ennico, K., Keller, L., Adams, J., et al. 2007, BAAS, 211, 1114
Ennico, K. A., Keller, L. D., Mar, D. J., et al. 2006, Proc. SPIE, 6269, 57
Gehrz, R. D., Becklin, E. E., De Buizer, J., et al. 2011, Adv. Space Res., 48, 1004
Gustafsson, B., Bell, R. A., Eriksson, K., & Nordlund, A. 1975, A&A, 42, 407
Herter, T. L., Adams, J. D., De Buizer, J. M., et al. 2012, ApJ, 749, L 18
Keller, L. D., Herter, T. L., Stacey, G. J., et al. 2002, Proc. SPIE, 4014, 86
———. 2004, Proc. SPIE, 5492, 1086
Lord, S. D. 1992, NASA Technical Memorandum 103957
Müller, T. G., Lagerros, & J. S. V. 1998, A&A, 338, 340
———. 2002, A&A, 381, 324
Pirger, B., Schoenwald, J., Herter, T., et al. 2006, Proc. SPIE, 6276, 29
Plez, B., Brett, J. M., & Nordlund, A. 1992, A&A, 256, 551
Roellig, T. L., Yuen, L., Sisson, D., & Hang, R. 2012, BAAS, 220, 135.08
Sloan, G. C., Kraemer, K. E., Price, S. D., & Shipman, R. F. 2003, ApJS, 147, 379
Tokunaga, A., & Vacca, W. 2005, PASP, 117, 421
Young, E. T., Becklin, E. E., Marcum, P. M., et al. 2012, ApJ, 749, L 17